Experiments on the stability and drag of a flexible sheet under in-plane tension in uniform flow

M.T. Morris-Thomas[*], S. Steen

Department of Marine Technology, Norwegian University of Science and Technology, Otto Nielsens vei 10, Trondheim NO-7491, Norway

Abstract

A flexible sheet in uniform parallel flow is studied in order to quantify its fluid dynamic drag and fluid–elastic stability characteristics. An experimental campaign is undertaken that involves a cantilevered sheet in air flow characterised by Reynolds numbers of order $R = 10^4 - 10^6$. The properties of the sheet include: constant mass per unit area; small but finite flexural rigidity; varying aspect ratios from within the range $0.43 < l/L < 1$, where L and l denote the length and width, respectively; and tension applied at the trailing edge. The unique aspect of the present work is an investigation into the influence of in-plane tension on both the fluid drag and fluid–elastic stability of the sheet. In the absence of tension, the configuration resembles a flag and the drag coefficient is observed to decrease with increasing aspect ratio and Reynolds number. In the presence of tension, the fluid drag is significantly reduced in the region below the critical flow velocity at which convected wave instabilities appear. This critical flow velocity can be increased through the moderate application of in-plane tension. Under lateral tension, the drag of the sheet is given to good approximation by the turbulent boundary layer drag law for a flat plate. Once stability is lost, however, the drag coefficient increases rapidly with Reynolds number due to convected waves travelling over the sheet's surface.
© 2009 Elsevier Ltd. All rights reserved.

Keywords: Fluid–elastic stability; Fluid drag; Uniform flow; Flexible sheet; In-plane tension

1. Introduction

Through casual observation of a flag, otherwise known as a flexible sheet, suspended in a breeze, the fluid–elastic instability known as flutter is clearly visible. This problem first gained attention through Rayleigh (1879) who considered a massless tension-free surface of infinite length in an effort to understand flag flutter. During a flutter episode, the flag extracts energy from the fluid, resulting in dispersive waves that originate at the leading edge and propagate towards the trailing edge with increasing amplitude. This oscillatory motion consequently affects the fluid dynamic drag which is expected to increase once stability is lost and the frontal area exposed to the flow increases. Although a flag in air flow is a familiar example of a fluid–elastic system, there are many other examples and applications—the propulsion of fish (Daniel, 1984), the dynamics of towed underwater cables (Dowling, 1988) and sheets, the biological mechanisms behind snoring (Huang, 1995), filaments (Schouveiler et al., 2005; Zhang et al., 2000), paper flutter in processing and printing (Watanabe et al., 2002), drag stabilisation (Auman and Wilks, 2005), and

---

general slender structures in axial flow (Païdoussis, 2004) to name but a few—that motivate a study on fluid–elastic instabilities of flexible sheets. However, what has received limited treatment throughout available literature, is the influence of in-plane tension on a flexible sheet in flow. Additional rigidity through tension is expected to stabilise the sheet's fluid–elastic response and consequently reduce its fluid dynamic drag. These effects are investigated here.

A classical flutter-type instability of a flexible sheet of small but finite thickness occurs when some threshold of the incident fluid velocity or perturbation of the system is breached. The point at which this occurs is termed the critical velocity U_c. In contrast to a forced excitation, such as the reattachment of shear layers (Allen and Smits, 2001) or though mechanical means (Taneda and Tomonari, 1974), we are concerned with a self-excited response. This is often characterised by convected waves or so-called limit-cycle oscillations [see Connell and Yue (2007), Tang et al. (2003), Zhu and Peskin (2002), among others]. The nature of the problem dictates that it is fully coupled whereby the properties of the sheet and the surrounding fluid are equally important and intimately linked to the sheet's response. Both stability and the subsequent magnitude and frequency of the instability depend on a competition between the fluid's momentum and the sheet's inertia, and the restorative influences of the sheet's flexural rigidity and any in-plane tension—which can be supplied by either the boundary layer or by external means. End-point boundary conditions also play an important role; from free–free conditions that resemble fish like swimming (Farnell et al., 2005), to clamped-free restraint indicative of a flag suspended in flow (Fitt and Pope, 2001).

To aid in our physical understanding, the character of the flow surrounding the sheet can be divided into two separate regimes based on the aspect ratio $\mathscr{A} = l/L$, where l and L denote the sheet width and length, respectively. For $\mathscr{A} \ll 1$, we essentially have a long slender sheet and the flow about it can be considered approximately two-dimensional in the cross-flow direction (Lighthill, 1960). Here, flow separation at the trailing edge is of little consequence compared to boundary layer-induced tension and added mass effects. In this regime, U_c decreases as the aspect ratio increases, and some success has been achieved at predicting U_c via a slender body formulation [see Lemaitre et al. (2005), Souilliez et al. (2006), for instance].

On the other hand, when $\mathscr{A} = \mathscr{O}(1)$, the characteristics of the flow are far more complicated due to the three-dimensionality of the sheet and the importance of flow separation and shear layers in the form of an unsteady wake and downwash over the cross-flow direction. In a strictly two-dimensional setting, the effect of an unsteady wake on a sheet of infinite width has been considered both theoretically [see Argentina and Mahadevan (2005), Huang (1995), Tang and Païdoussis (2008), Zhu and Peskin (2002), among others] and experimentally in the soap film experiments of Zhang et al. (2000). The study by Tang and Païdoussis (2008) demonstrates that the wake is of little consequence to stability when the sheet is considered long.[1] However, for a sheet of finite width, it is generally understood that it will be theoretically more stable than its two-dimensional counterpart (Eloy et al., 2007). The coupling of unsteadiness with three-dimensionality has only recently been approached numerically (Tang et al., 2003) with some success at determining the critical flow velocity and the sheet's qualitative behaviour after stability is lost.

The distinctive feature of a flexible sheet is its low flexural rigidity. This feature complicates any experimental study where it is important for the sheet to maintain a planar form with little or no geometric irregularities as the flow velocity is increased up to, and beyond, the critical velocity. To circumvent this, most authors choose to study a sheet mounted vertically (Datta and Gottenberg, 1975; Lemaitre et al., 2005; Taneda, 1968) allowing gravity to impose a linearly varying axial tension that reduces to zero at the trailing edge. This gravity-induced in-plane tension dominates over the minimal amount provided by fluid friction under realistic flow conditions (Lemaitre et al., 2005). Alternatively, one may mount a sheet horizontally in flow and employ sufficient in-plane tension or so-called pre-tension (Coene, 1992; Morris-Thomas and Steen, 2008; Watanabe et al., 2002; Yamaguchi et al., 2003) to ensure a planar sheet form up to the critical flow velocity.

Although applying in-plane tension to a flexible sheet is convenient for experiment, it does however replicate some important practical applications; for instance, print media and paper manufacture, and aircraft towed advertising banners. In printing and paper manufacture, knowledge of the stability characteristics of the sheet are important; for towed banners on the other hand, fluid dynamic drag reduction assumes priority over convected ripple like modes.[2] In the context of pure transverse tension (cross-flow normal) applied to a simply supported sheet, Watanabe et al. (2002) demonstrates an elevated critical velocity by suppressing lateral sheet displacements. Moreover, Watanabe et al. (2002) present some revealing illustrations that show the flow surrounding a sheet in the presence of pure lateral restraint to be largely two-dimensional, distinctly unseparated, with progressive flexural waves exhibiting a remarkable similarity to those of a cantilevered pipe conveying fluid. In contrast, but with similar conclusions, Coene (1992)

---

[1]The term 'long' is subjective in a two-dimensional setting. Tang and Païdoussis (2008) cite a mass ratio of $\rho L/M > 4$ to distinguish a long two-dimensional sheet—ρ being the fluid density and M the sheet's mass per unit length.

[2]These ripple like modes resemble the wrinkles which appear across the surface of membranes under in-plane tension [see Wong and Pellegrino (2006)].

examined a free–free paper sheet of $\mathscr{A} = \mathcal{O}(0.1)$ with tension supplied axially (normal to the trailing edge). A clear increase in the critical velocity is shown. However, given that the sheet's flexure was not defined, coupled with the inherent anisotropy of paper, any direct comparison with existing or new data is speculative at best.

The fluid dynamic drag of a sheet is expected to increase once stability is lost to flutter (Taneda, 1968). This is because: the frontal area exposed to the flow increases in the presence of flexural waves and the wake transforms from a well defined von Kármán vortex street to one comprising large eddy formations (Taneda, 1968, especially Fig. 13). While this phenomenon has been demonstrated for laminar flows with in-plane tension provided by gravity (Taneda, 1968), its observation in turbulent flows of more practical interest has suffered because of geometric irregularities of the sheet up to the point of instability [see Auman and Dahlke (2001), Carruthers and Filippone (2005), Fairthorne (1930)]. Like a flat plate, the drag coefficient of a flexible sheet decreases with increasing aspect ratio (Auman and Dahlke, 2001; Carruthers and Filippone, 2005; Taneda, 1968); and, furthermore, we can expect its magnitude to approach that of a flat plate under sufficiently small elastic deformations. To the authors' knowledge, the effect of additional rigidity through in-plane tension, although likely to postpone an expected rise in the drag coefficient at the onset of a fluid–elastic instability, has hitherto not been studied.

The present paper examines a rectangular flexible sheet of small flexural rigidity in uniform parallel flow. The leading and trailing edges of the sheet comprise clamped and free boundary conditions, respectively. Our primary goal is to address the issue of in-plane tension and its impact on both the fluid–elastic stability and fluid dynamic drag characteristics of the sheet. An experimental campaign is undertaken whereby the sheet's dimensions are chosen such that $0.43 < \mathscr{A} < 1$. In-plane tension is applied to the sheet at a given angle θ to the trailing edge. The magnitude of this tension is varied from zero (a flag) to values in the region where tension-induced rigidity is expected to dominate over flexure. The instability we are concerned with is of the flutter-type which is characterised by convected waves propagating from the leading to the trailing edge of the sheet's surface. However, under certain conditions transverse mode shapes are possible. The paper is organised as follows: appropriate scalings and an approximate analytical model describing the instability of a flexible sheet are presented in Section 2; the experimental campaign undertaken is described in Section 3; results pertaining to the flutter-type instability in Section 4.1, the fluid dynamic drag in Section 4.2 and the fluid dynamic drag in the presence of in-plane tension in Section 4.3 are then discussed; and finally, conclusions are provided in Section 5.

2. Scaling and a qualitative model

We first consider a simple two-dimensional analytical model of a flexible sheet. This enables us to construct a consistent set of dimensionless parameters, and facilitates an understanding of how these parameters affect a flutter-type instability. This approach is motivated by Coene (1992) and Shelley et al. (2005) and we combine their ideas to include linear elastic deformation of the sheet due to both flexure and axial tension.

We consider a flexible sheet of length L comprising an isotropic material of mass per unit area M immersed in an ideal fluid in the presence of uniform parallel flow of velocity U. The flow approaches from $X = -\infty$ and we assume that the sheet occupies the plane $Y = 0$ in its quiescent position. The vertical displacement of the sheet from its mean position is denoted by $w(X, t)$, which we assume small—$w \ll \lambda$, λ being a typical wavelength, or $w \ll L$, L being the sheet length. This assumption is justified given that we are only interested in the stability criteria, rather than post-stability behaviour, of the sheet. Under the restriction of linear elasticity, the vertical displacement of the flexible sheet is governed by

$$B \frac{\partial^4 w}{\partial X^4} - T \frac{\partial^2 w}{\partial X^2} + M \frac{\partial^2 w}{\partial^2 t} = \Delta P(X; t), \tag{1}$$

which is essentially the classical Euler–Bernoulli beam equation with an additional term accounting for axial tension per unit width of the sheet T. The fluid pressure acting across the sheet is denoted $\Delta P(X; t)$ and $B = Eh^3/12(1 - v^2)$ defines the flexural rigidity, where h is the sheet thickness, E the elastic modulus, and v denotes Poisson's ratio.

We now assume a harmonic response of the sheet, and that the amplitude of this response is much smaller than the sheet length. Its linear displacement from the mean position $Y = 0$ can then be written

$$w(X, t) = A \exp(iKX - i\Omega t), \tag{2}$$

where K denotes the spatial wavenumber and Ω the circular wave frequency. In adopting (2), we are essentially implying that $\lambda \ll L$, which is an obvious simplification. However, this is justified given our motivation involves identifying consistent scaling parameters and deducing their qualitative contribution to the sheet's stability.

Under the assumption that the sheet motion and zero flux boundary condition are linear about the plane $Y = 0$, the appropriate form of the fluid pressure, in accordance with (2), acting across the sheet is [cf. Lamb (1932), Art. 232]

$$\Delta P(X;t) = 2\frac{\rho}{|K|}(\Omega - UK)^2 w, \tag{3}$$

where $|K| \equiv \sqrt{K^2}$. In scaling the governing equation, it is convenient to adopt:

$$X = xL, \quad w = \eta L, \quad t = \tau\frac{L}{U}, \quad K = \frac{k}{L}, \quad \Omega = \omega\frac{U}{L}, \quad \Delta P = \rho U^2 \Delta p. \tag{4}$$

Introducing these into the governing equation (1) with (3) provides

$$\eta_{\tau\tau} + \frac{1}{v^2}\eta_{xxxx} - \kappa\eta_{xx} = 2\frac{\mu}{|k|}(\omega - k)^2\eta, \tag{5}$$

which describes the displacement of the sheet in terms of three dimensionless quantities defined as follows:

$$\mu = \frac{\rho L}{M}, \quad v = U\left(\frac{ML^2}{B}\right)^{1/2}, \quad \kappa = \frac{T}{MU^2}. \tag{6}$$

The first parameter, μ, describes the ratio of fluid forcing to the inertia of the sheet with time scaled as $t(U/L)$, and the second, v, is commonly referred to as the reduced velocity and is essentially the ratio of time scales between the elastic deformation due to flexure and that which results from the fluid's forcing (Tang and Païdoussis, 2008). The third parameter, κ, is essentially the ratio of time scales between the elastic deformation due to fluid forcing and the elastic deformation due to tension. These three parameters can be combined to produce:

$$\frac{v}{\mu} = U\left(\frac{M^3}{\rho^2 B}\right)^{1/2}, \quad \beta = \kappa v^2 = \frac{TL^2}{B}. \tag{7}$$

The utility of which is that v/μ effectively removes the dependence on sheet length from the scaled fluid velocity. This form was employed by Tang and Païdoussis (2008) and it is also the appropriate velocity scaling for an infinitely long flexible plate under fluid loading [cf. Crighton and Oswell (1991)]. The advantage of β is that we have effectively removed the dependence on fluid velocity from the dimensionless tension so that we now have a direct measure of the deformation due to tension with that from flexure. This form appears in the study conducted by Yamaguchi et al. (2003) for simply supported sheets. We should also point out that although β in (7) is derived by assuming that T acts in the axial direction, we can also employ this definition for β when T is applied at an angle θ to the trailing edge of a three-dimensional sheet (cf. Section 3). In which case, T is understood to be the magnitude of the in-plane tension.

We now construct a dispersion relation connecting the normalised circular frequency ω and wavenumber k by placing (2) in (5), whence

$$\mathscr{D}(k,\omega) = \omega^2 - \frac{1}{v^2}(k^4 + \beta k^2) + 2\frac{\mu}{|k|}(\omega - k)^2 = 0, \tag{8}$$

where $\beta = \kappa v^2$. A dispersion relation of similar meaning to Eq. (8) is presented in Shelley et al. (2005) with axial tension omitted but intimated in the form of a Blasius friction law. By replacing β with $\beta = 1.3\text{R}^{-1/2}L^2/B$, where R denotes the Reynolds number, this later form appears in Connell and Yue (2007) for constant R. Here, however, we leave the magnitude of β unspecified.

In solving the dispersion relation for ω we arrive at

$$\omega^{\pm} = \frac{k}{|k| + 2\mu}\left\{2\mu \pm \frac{\sqrt{|k|}}{v}[k^2|k| + \beta|k| - 2\mu v^2 + 2\mu k^2 + 2\mu\beta]^{1/2}\right\} \tag{9}$$

for any real-valued $k = n\pi$ with $n \in \mathbb{N}$. It is interesting to note that (9) is not too dissimilar to the dispersion relation for a Kelvin–Helmholtz type instability of a two layer inviscid fluid, whereby the restorative influences of sheet flexure and axial tension are analogous to buoyancy and surface tension, respectively.

To determine instability, we search for frequencies which exhibit spatially growing modes whereby $\mathfrak{I}(\omega) > 0$ is required. Consequently, in (9) we set the terms enclosed in square braces to zero and find that

$$v_c^2 > (1 + |k|/2\mu)(k^2 + \beta) \tag{10}$$

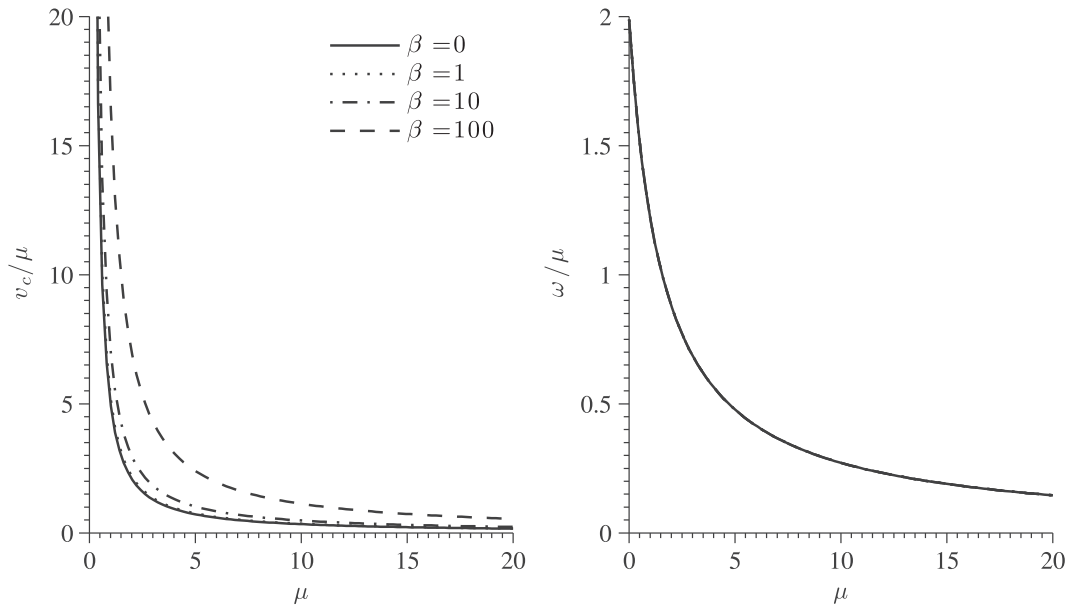is required to realise instability of the flutter-type through convected flexural waves.

Fig. 1. Left axis: the critical velocity $v_c/\mu = U(M^3/\rho^2 B)^{1/2}$ plotted against the mass ratio $\mu = \rho L/M$ for the first eigenmode $k = \pi$ of a flexible sheet under axial tension $\beta = \kappa v^2$ in uniform flow. Right axis: the corresponding circular frequency $\omega/\mu = \Omega(M/\rho U)$ at the point of instability.

Eqs. (9) and (10) with $k = \pi$ are plotted in Fig. 1, where we have chosen to scale the ordinate of each by μ which conveniently collapses the data. The role of β is to postpone instability; so that for $\beta = 100$, for instance, v_c/μ has increased by a factor of approximately 3.5 over $\beta = 0$. The fact that β does not affect ω/μ at the point of instability will come as no surprise, given the form of (9).

For practical purposes we can write (10) in dimensional form,

$$U_c^2 > \frac{|K|}{2\rho M}(M + 2\rho/|K|)(BK^2 + T), \tag{11}$$

which serves to illustrate the effects of both structural and added mass, flexure, and axial tension on stability.

Despite their simplicity, Eqs. (9)–(11) illustrate some important aspects of the system. Firstly, any increase in the length of the sheet will destabilise the system—this effect is of $\mathcal{O}(L^3)$ which is quite disastrous from a practical standpoint. Both flexural rigidity and tension act to stabilise the sheet and any increase will be coupled by an increase in both U_c and ω meaning the fluid must supply more energy to excite a fluid–elastic response. On the other hand, an increase in either structural or fluid added mass, determined by $2\rho/|K|$, will promote instability. Another important point, first mentioned by Zhu and Peskin (2002) and more recently by Connell and Yue (2007), is that a massless system is infinitely stable. This is clearly demonstrated by (11) where $U_c \to \infty$ as $M \to 0$. Lastly, it is worth pointing out that with axial tension replaced by a constant flow-induced tension from a Blasius boundary layer drag law [cf. Connell and Yue (2007)], it contributes $\beta \approx \mathcal{O}(1)$ and therefore provides minimal additional stability when compared to an externally applied tension.

3. Experiments

We now outline the experimental campaign undertaken to investigate the drag and stability of a rectangular flexible sheet in uniform flow. The experimental campaign was conducted in the low speed wind tunnel of the Aerodynamics Laboratory at the Norwegian University of Science and Technology. The tunnel comprises an available test-section of $2.7\,\text{m} \times 1.83\,\text{m}$ and allows fluid velocities up to $30\,\text{m s}^{-1}$ with a turbulence intensity of less than 5%. The sheet was mounted vertically along the centre-line of the test-section with a clamped leading edge and free trailing edge. A diagram of the test set-up is provided in Fig. 2 which we shall now explain in the following subsections.
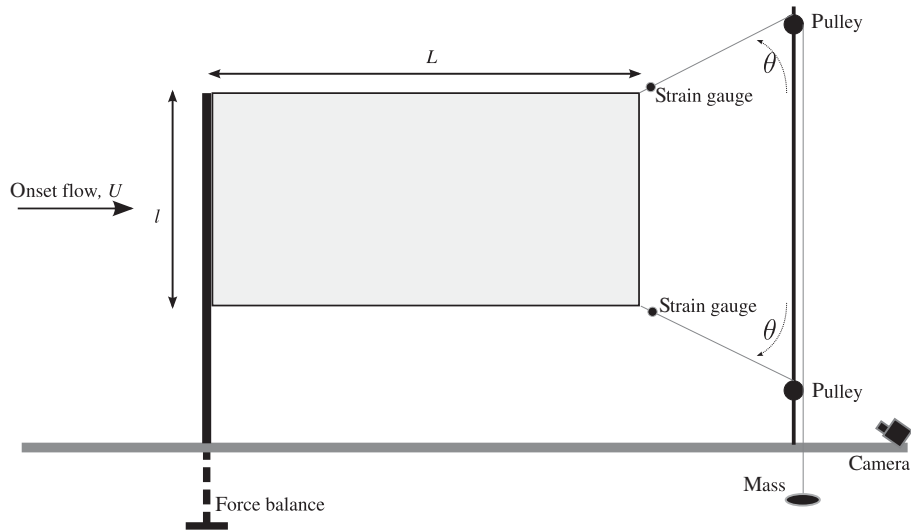
Fig. 2. A schematic of the test set-up. The wind tunnel floor is represented by the grey horizontal line.

Table 1
Characteristics of the sheets employed in the test matrix where $\mathscr{A}$ denotes the aspect ratio, A the projected surface area, $\mu = \rho L / M$ the mass ratio, $v = U(ML^2/B)^{1/2}$ the reduced or normalised incident flow velocity, $\kappa v^2 = TL^2/B$ the ratio of tension to flexure, R the Reynolds number, and θ represents the angle of application of tension at the trailing edge.

Sheet	$\mathscr{A}$	A (m^2)	μ	v	κv^2 ($\times 10^3$)	R ($\times 10^5$)	θ
S1	1.0	0.563	6.410	23.0–434	19.4–75.0	0.315–5.95	0
S2	0.75	0.750	8.546	37.4–549	34.5–133	0.513–7.53	0, 22.5°, 45°
S3	0.60	0.938	10.68	43.2–599	54.0–208	0.592–8.21	0, 22.5°, 45°
S4	0.50	1.125	12.82	56.2–744	77.7–300	0.770–10.2	0, 22.5°, 45°
S5	0.43	1.312	14.96	63.8–977	106–408	0.875–13.4	0

3.1. Apparatus

A transparent polyethylene material of thickness $h = 0.15$ mm was chosen for the sheet as it provided a reasonably low mass per unit area $m = 0.141$ kg m^{-2} and sufficient bending rigidity $B = 59.65 \times 10^{-6}$ N m^2/m to allow an observation of flexural waves. Using a width of $l = 75$ cm, the length of the sheet was varied to produce five aspect ratios from within the range of $0.43 < \mathscr{A} < 1$. These five geometries are hereafter denoted by S1, S2, S3, S4, and S5. The characteristics of which are summarised in Table 1. With these dimensions, Reynolds numbers were in the order of R $= 10^4 - 10^6$—a range which encompasses the transitional regime for the boundary layer on a flat plate. In addition to the aspect ratio, the other parameters varied were the magnitude of the in-plane tension T and the angle θ at which it was applied to the trailing edge.

At the corners of the trailing edge, tension was applied. This was accomplished with two lengths of Kevlar string attached to two sets of known and equal weights. These weights were parametrically varied to produce a combined pre-tension in the order of 1–15 N. To achieve a constant mean tension throughout a test run, each string travelled through a pulley system that directed it underneath the wind tunnel where it was attached to the weights. The position of the pulleys was varied to produce three different angles at which the string left the trailing edge: $\theta = 0$, 22.5°, and 45°; whereby $\theta = 0$ implies a perpendicular tension to the trailing edge. The tension in each string was measured directly behind the trailing edge of the sheet with two ring type strain gauges surrounded by swivels to avoid excessive rotations. The strain gauges were calibrated with an expected error in the order of ± 0.01 N. The applied tension produced a small oscillatory out-of-plane component when the sheet experienced flutter. At worst, its amplitude was around 7% of the total in-plane tension at $U = 12$ m s^{-1} for S5. The magnitude of the out-of-plane component decreased for increasing $\mathscr{A}$ such that for S1 and S2 its amplitude was less than $0.01 T$ at the maximum flow velocity considered here.

A three-component force balance, situated underneath the centre of the test-section, was employed to measure the in-line force. This was accomplished by utilising a vertical pole, cantilevered from the force balance, that extended into the

centre of the test-section. Along the leading edge, nylon tape was employed, affixing the sheet to the pole and simulating a clamped boundary condition. To minimise its drag contribution and affect on the fluid–elastic deformation of the sheet, the vertical pole, of height 1.43 m, comprised an elliptical cross-section ($a = 4$ cm and $b = 2$ cm). The bottom of each sheet was located 54 cm above the base of the wind tunnel. This was deemed sufficient to avoid the developing turbulent boundary layer along the wind tunnel floor and walls—of thickness $\delta \approx 15$ cm at the leading edge location, and, assuming a logarithmic velocity profile, climbing to approximately 17 cm at the trailing edge position.

The incident flow velocity was obtained via a Pitot-static tube fixed 28 cm from the roof of the wind tunnel. At an air temperature of 22.1 °C, the properties of the fluid used throughout the experiments are $\rho = 1.205$ kg m^{-3} and $v = 0.150$ cm^2 s^{-1}. Measurements from the Pitot-static tube, force balance, and strain gauge channels were acquired through an HBM instrumentation amplifier attached to a notebook computer running customised data acquisition software. All data was digitised at 200 Hz and pre-processed through a low-pass Butterworth filter at 40 Hz to avoid ambient noise. In addition, each run was recorded at 30 frames per second with a digital camera situated 44cm behind the trailing edge position on the wind tunnel floor.

Initial testing revealed the drag coefficient of the mounting pole to be $C_D = 0.59$. Hence, the independent drag contribution of the pole ranged from 0.003 N at 0.5 m s^{-1} quadratically climbing to a maximum of 1.59 N at 12 m s^{-1}— the largest fluid velocity examined here. We expect that the addition of the attached sheet to the pole has the effect of a splitter plate and will therefore reduce the drag contribution of the pole further. Using a circular cylinder and splitter plate configuration as a guide (Hoerner, 1965, § 3–6), we can infer a conservative lower bound of $0.6C_D$ for the portion of the pole comprising the attached sheet. We can therefore expect a drag reduction by the presence of the sheet by, at most, 21% of the total pole drag. To place this into perspective, this amounts to, at worst, approximately 3% of the total measured drag force of the sheet at $U = 12$ m s^{-1}. Moreover, we suspect that given the elliptical cross-section of the pole, combined with the flexibility of the sheet allowing some momentum exchange in the wake at the onset of flutter, the drag reduction experienced by the pole will be somewhat smaller than our 21% upper bound. This effect is not corrected for in the data analysis implying that the calculated drag of the sheet will be slightly smaller than expected.

A typical test run commenced from rest and the flow velocity of the wind tunnel gradually increased over increments of approximately 0.2−0.5 m s^{-1}. This continued beyond the onset of the first observed convected wave mode, until wild oscillations of the trailing edge ensued. At that point, the flow velocity was either terminated or gradually decreased over increments to cover the fluid–elastic instability region. Each run lasted for approximately 12–20 min, with time windows for each chosen fluid velocity, on average, 42.1 s in length with a standard deviation of 10.6 s. This process was repeated over the parameter space of the test matrix which included five sheet geometries, three angles, and four to seven different magnitudes of trailing edge tension.

3.2. Data analysis and processing

Each data set was separated into time windows of length determined from the velocity profile incident on the sheet. After windowing, a general Fourier transform was performed to determine the average flow velocity, in-line force, and trailing edge tension for each time window. Moreover, the available frequency information allowed us to determine the dominant harmonics of the trailing edge tension and in-line force. The fluid–elastic instability was clearly observable from the trailing edge tension where the magnitude of the first harmonic increased by a factor of approximately 10 over one velocity increment once stability was lost. At this point, the Strouhal number, based on the length of the sheet ($St = fL/U$), was in the order of 0.4–0.6—around half the value reported by Shelley et al. (2005) for a cantilevered sheet in water with $\beta = 0$. As the flow velocity was increased beyond critical, St increased in a linear fashion to a peak of around 2.2–3.0 with the lower limit occupied by data sets comprising the largest in-plane tensions explored here.

The drag experienced by the sheet was determined from the in-line force measured at the force balance with the drag from the pole and total horizontal tension at the trailing edge subtracted. The drag force, denoted F_D, was then normalised according to $C_D = F_D/0.5\rho A U^2$ where A is the surface area of the sheet and U the flow velocity. The flow velocity, determined from the pressure measured by a Pitot-static tube, over each time window comprised a standard deviation of less than 0.05 m s^{-1} from the mean for $U > 2.4$ m s^{-1}. Below this range, however, the flow velocity showed some variability with the standard deviation increasing to 0.19 m s^{-1} in some cases.

4. Results and discussion

A selected run from the experiments is illustrated in Fig. 3 which shows the incremental increase in fluid velocity and subsequent oscillatory behaviour of the forces measured in-line and at the trailing edge once stability is lost to flutter.
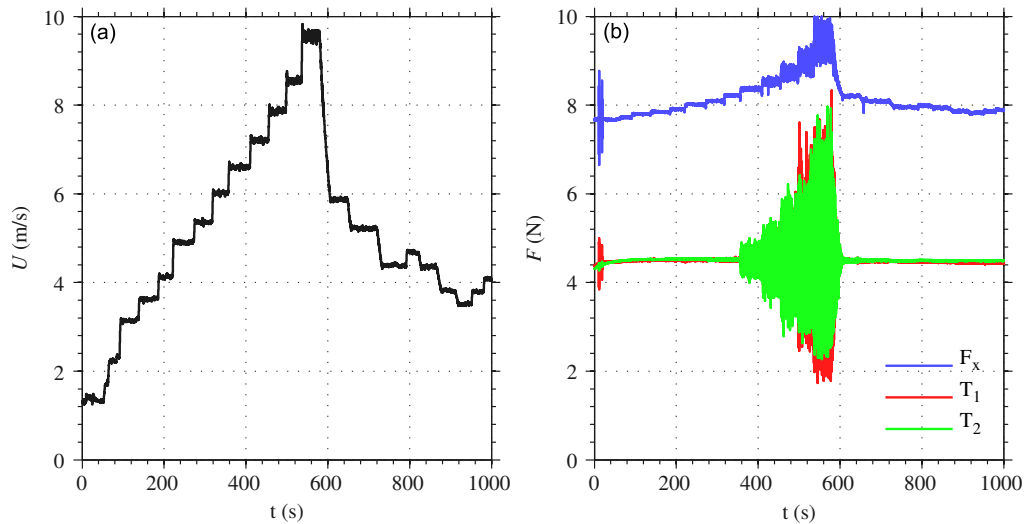
Fig. 3. A typical time series for S2 (0.75 m × 1.25 m) with tension applied at 22.5° to the trailing edge: (a) illustrates the incident flow velocity and (b) shows the forces measured: in-line F_x; at the upper strain gauge T_1; and at the lower strain gauge T_2.

The behaviour illustrated in the plot once stability is lost, matches our observation of surface waves convected from the leading to the trailing edge of the sheet. The time series results presented in Fig. 3 are quite typical of all cases considered throughout the experimental campaign. Frequency analysis of the time-windowed data indicates that the first modal frequency of the dominant convected wave event is in the order of 1–10 Hz at the point of instability. The effect of which is transferred to both the force balance and strain gauges at the trailing edge (cf. Fig. 3). Rather than growing in time, these oscillations, which are steady and well defined, grow in amplitude and frequency as the fluid velocity is increased further beyond the first observed instability. When this occurs, a linear dispersion relation can no longer relate the frequency and wavenumber of the flexural waves as elastic nonlinearities, such as curvature, become important. These nonlinearities will act to limit the amplitude of the instability. One could argue that this behaviour is in fact another stable state occupied before the sheet undergoes chaotic motion for flow velocities much larger than critical. However, we are not concerned with this chaotic motion at large fluid velocities here.

4.1. Fluid–elastic instability

We first examine loss of stability due to flutter. The critical velocity, denoted by v_c, was determined by examining the first harmonic of the trailing edge tension. A sharp jump in magnitude and phase shift of the first harmonic indicates stability loss and the appearance of convected waves. Figs. 4–6 illustrate the results obtained from this analysis for S2, S3, and S4, respectively. In each figure, the scaled velocity v_c/μ is plotted against the trailing edge tension for $\theta = 0°$, 22.5°, and 45°. We represent the tension by the parameter combination $\beta/\mu^2 = T(M^2/\rho^2 B)$, where T is the tension applied by the weight and the multiplicative factor $M^2/\rho^2 B$ is constant throughout; the utility of which removes the dependence of sheet length and fluid velocity from the scaled tension and allows us to examine the effect of pure tension across each sheet considered. For comparative purposes, we include the stability boundary determined from the linear dispersion relation (10) for the first oscillatory mode $k = \pi$.

It is important to note that the exact instability boundary is not definitive in practice. There is a small but finite range of fluid velocities at which the sheet can undergo periods of both stable and unstable oscillatory motion. The transferal between these two states does not appear to be related to any of the input variables examined here. This bi-stability could be memory-dependent, such as that demonstrated numerically by Zhu and Peskin (2002) and experimentally by both Watanabe et al. (2002) and Souilliez et al. (2006), or perhaps it may originate from perturbations of the flow velocity and any residual turbulence available. The dynamics of the system within this region are unclear and, in Figs. 4–6, we account for this uncertainty by incorporating a shaded region where upper and lower bounds of v_c are indicated by shape preserving polynomial interpolants.

The experimental results for v_c indicate that instability can be postponed by increasing the in-plane tension. In most cases we observe a monotonic increase in v_c/μ with increasing β/μ^2. Apart from a persistent vertical offset, this trend is partially captured by the qualitative expression for v_c (10). We suspect that this offset emerges from our limited
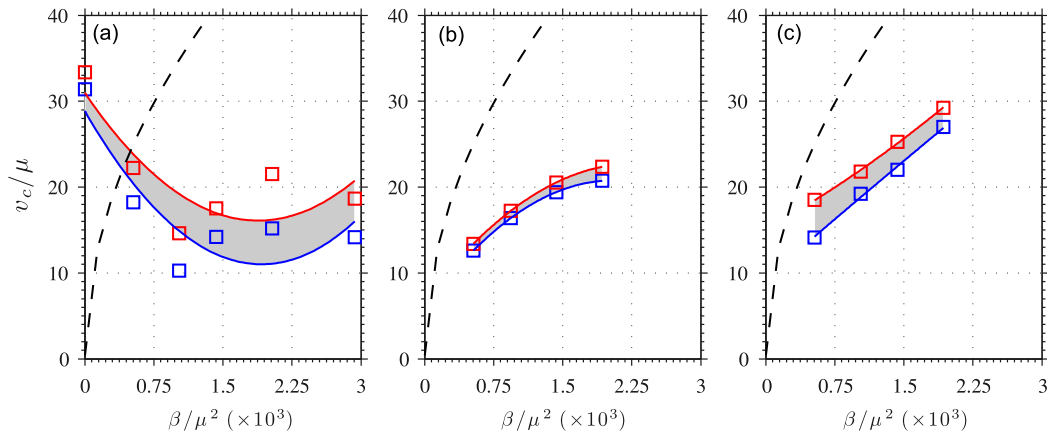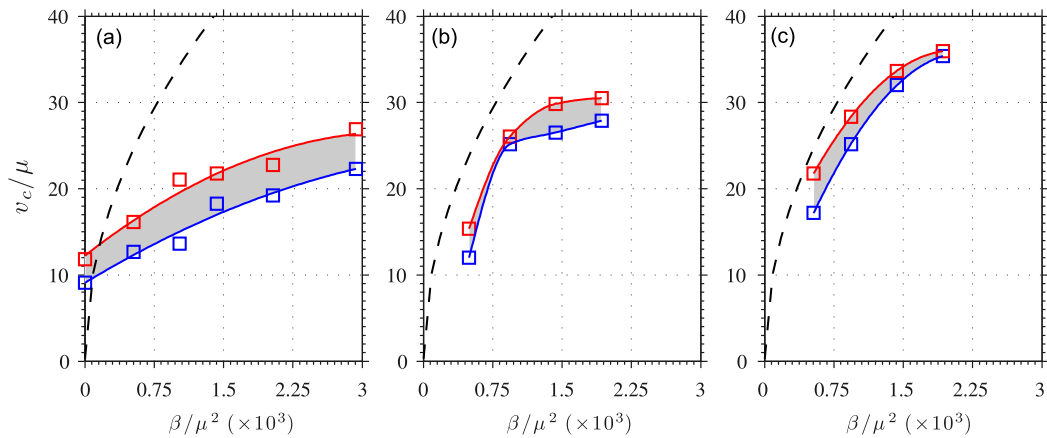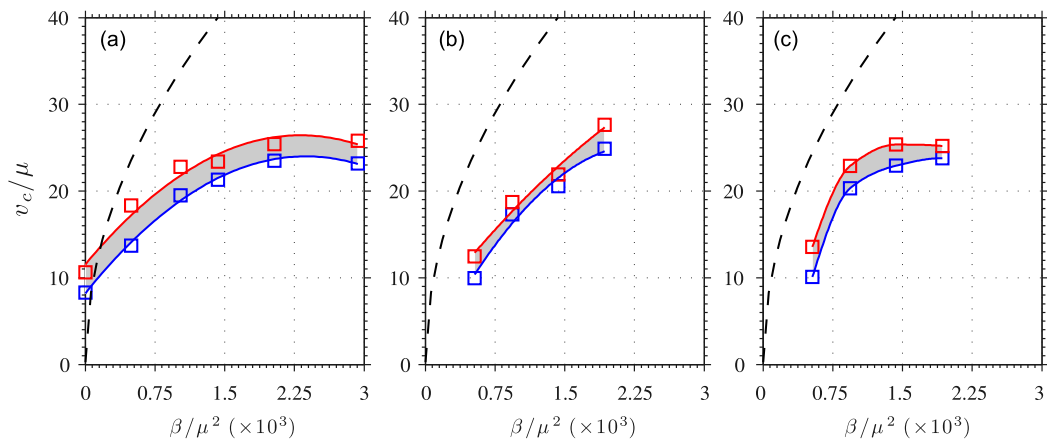
Fig. 4. S2: $\mathscr{A} = 0.75$. The measured critical flow velocity $v_c/\mu = U(M^3/\rho^2 B)^{1/2}$ plotted against trailing edge tension $\beta/\mu^2 = T(M^2/\rho^2 B)$ applied at angles of: (a) $\theta = 0$; (b) $\theta = 22.5°$; and (c) $\theta = 45°$. The dashed line corresponds to Eq. (10).

Fig. 5. S3: $\mathscr{A} = 0.60$. The measured critical flow velocity $v_c/\mu = U(M^3/\rho^2 B)^{1/2}$ plotted against trailing edge tension $\beta/\mu^2 = T(M^2/\rho^2 B)$ applied at angles of: (a) $\theta = 0$; (b) $\theta = 22.5°$; and (c) $\theta = 45°$. The dashed line corresponds to Eq. (10).

Fig. 6. S4: $\mathscr{A} = 0.50$. The measured critical flow velocity $v_c/\mu = U(M^3/\rho^2 B)^{1/2}$ plotted against trailing edge tension $\beta/\mu^2 = T(M^2/\rho^2 B)$ applied at angles of: (a) $\theta = 0$; (b) $\theta = 22.5°$; and (c) $\theta = 45°$. The dashed line corresponds to Eq. (10).

description of the fluid added mass which appears in the dispersion relation. The qualitative theory assumes that the fluid pressure is composed of one single spatial mode that obeys only a periodicity condition at the sheet end-points. In reality, however, the first modal frequency of the instability will comprise a number of spatial mode shapes.

In contrast to the above, the results pertaining to S2 with tension applied at $\theta = 0$ (cf. Fig. 4(a)) follow an entirely different trend. In particular, v_c measured at values of $\beta/\mu^2 = 0$ and 400 are exceptionally large in comparison to their companion data. The dynamics of the instability appear to be different and we present Fig. 7 to illustrate snap-shots of S2 with $\beta/\mu^2 = 400$ both before and after the appearance of convected waves. Although the left frame of Fig. 7 shows S2 to be stable to convected waves, we observe a transverse oscillation mode. The right frame, at a higher fluid velocity, clearly shows this transverse standing wave envelope which is now superimposed on a convected wave instability.
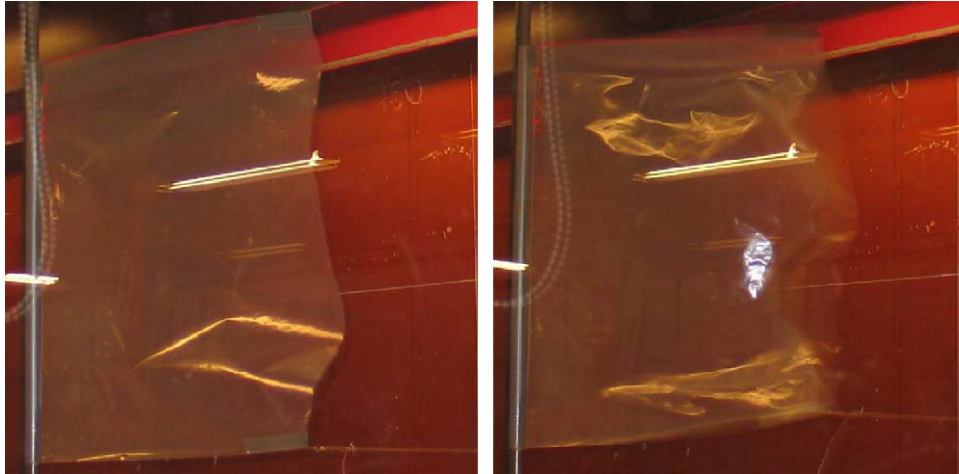

Fig. 7. S2 with trailing edge tension $\beta = 400$ applied at $\theta = 0$. A transverse mode is observed across the surface of the sheet. Left frame: $v < v_c$ and the right frame: $v > v_c$.
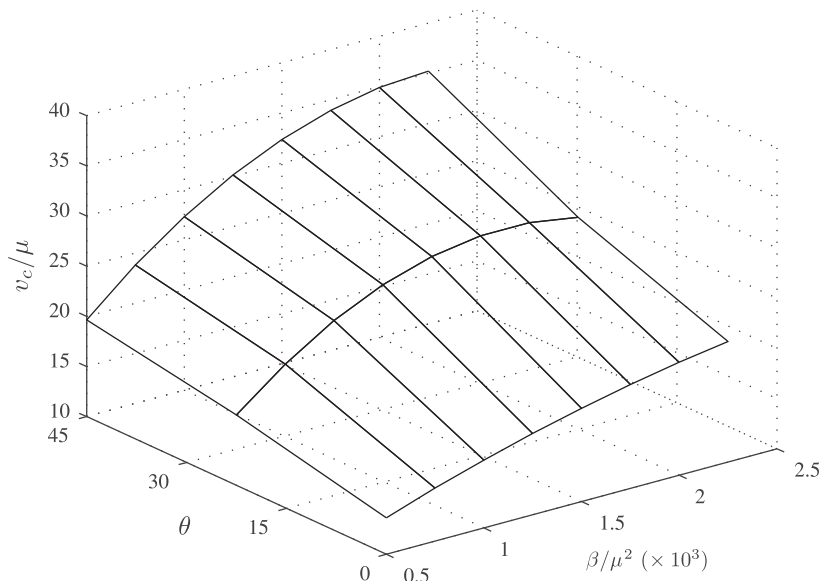

Fig. 8. A surface plot of the measured critical flow velocity $v_c/\mu = U(M^3/\rho^2 B)^{1/2}$ versus the in-plane tension $\beta/\mu^2 = T(M^2/\rho^2 B)$ and its direction θ. Cubic polynomial interpolates have been used along the β/μ^2 axis to re-grid the measured data for mean values of v_c. This plot pertains to S3 where $\mathscr{A} = 0.6$.

Its wave length is approximately $l/2$. These well defined transverse modes were observed only for the shortest sheets, $\mathscr{A} = 0.75$ and 1, where static deflection of the sheet due to its weight is minimal. Not surprisingly, with in-plane tension applied laterally ($\theta = 22.5°$ and $45°$), these transverse modes are suppressed (cf. Figs. 4(b) and (c)). Souilliez et al. (2006), in the context of flags with $\beta = 0$, suggests that such transverse modes and three-dimensionality can delay the onset of flutter by artificially increasing the rigidity of the system. This may well be the case because out-of-plane bending will increase the stiffness of the sheet to in-plane bending or, in our case, instability.

With the magnitude of the in-plane tension held constant, an increase in θ postpones instability. To emphasise this effect, we present Fig. 8 which shows a surface plot of v_c/μ for S3 using a cubic polynomial interpolant over the measured data presented in Fig. 5. The distinct trend of increasing stability with increasing θ, as demonstrated in the surface plot, is clearly reflected in the measured data for S2 and S3 (cf. Figs. 4 and 5)—note the values for v_c at $\beta/\mu^2 = 0$ and 400 in Fig. 4(a) defy this trend, but, as previously mentioned, the dynamics of the instability are different here because a transverse mode shape was excited. Moreover, if one excludes the values of v_c corresponding to $\beta/\mu^2 = 2200$ in Fig. 6(c), then S4 follows this trend also. For increasing θ, the in-plane tension comprises an increasing lateral component. Assuming that this suppresses three-dimensional geometric irregularities, or perturbations, then one can expect the sheet to adopt a more streamlined orientation and, consequently, an elevated stability. However, this trend is unlikely to continue for $\theta > 45°$ where increasingly less axial tension would be available to the sheet.

The effect of $\mathscr{A}$ on the sheet stability is difficult to determine from the present data set. In most cases, v_c is of the same order of magnitude for each sheet and no conclusions can be drawn.

4.2. Fluid dynamic drag of a flag

We now consider the fluid dynamic drag experienced by flexible sheet with $\beta = 0$—in other words, a flag. Measured results are plotted in Fig. 9 for $C_D = F_D/0.5\rho A U^2$ versus the Reynolds number, where the error bars of each data point correspond to the standard deviation of C_D for each time window. The results are presented for sheets with aspect ratios $\mathscr{A} = 1, 0.75, 0.6, 0.5, 0.43$. In addition to the present measurements, we compare with published data (Carruthers and Filippone, 2005) denoted 'CF' hereafter, for a cotton flag comprising aspect ratios $\mathscr{A} = 0.1, 0.05, 0.03$.
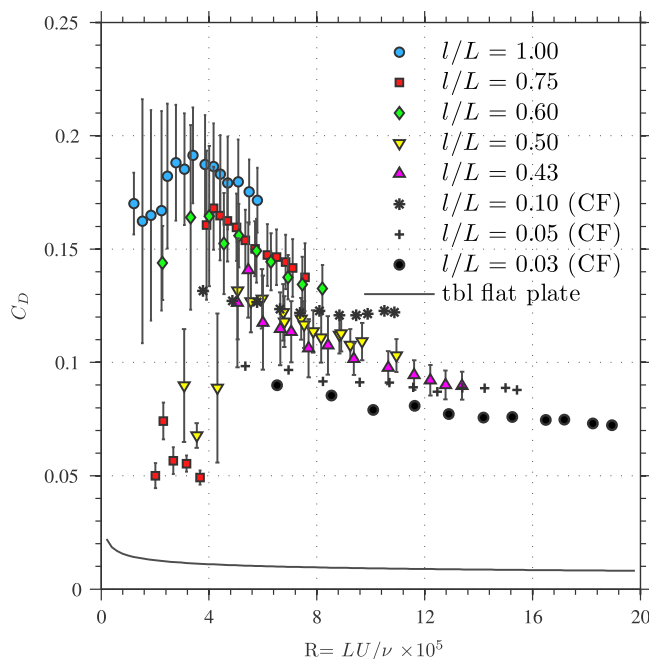

Fig. 9. The fluid drag in uniform flow experienced by a horizontal flag. The present measurements for a polyethylene sheet are plotted for five aspect ratios $\mathscr{A} = l/L$ with error bars corresponding to the standard deviation of C_D at each measured flow velocity. Published data (Carruthers and Filippone, 2005), denoted 'CF' for a cotton flag provide three additional values of $\mathscr{A}$. The solid line represents the expected fluid drag of a flat plate experiencing a turbulent boundary layer [cf. Schlichting and Gersten (2000), eqn. (18.99)].

For comparative purposes, Fig. 9 includes the expected fluid drag of flat plate experiencing a turbulent boundary layer in plane parallel flow [cf. Schlichting and Gersten (2000), pp. 580–586]:

$$C_D = 2\left[\frac{\kappa}{\ln R}G(\Lambda; D)\right]^2, \tag{12}$$

with

$$\Lambda = \ln R, \quad D = 2\ln \kappa + \kappa(C^+ - 3.0), \tag{13}$$

where the function $G(\Lambda; D)$ is determined from the numerical solution of (Schlichting and Gersten, 2000, eq. (17.60))

$$\frac{\Lambda}{G} + 2\ln\frac{\Lambda}{G} - D = \Lambda. \tag{14}$$

This friction law is valid for smooth and rough surfaces by judicious choice of C^+ for $R > 10^5$. Given that the sheet material is polyethylene, it is reasonable to assume a smooth surface and therefore $C^+ = 5.0$. The constant κ denotes the Kármán constant and takes the numerical value 0.41.

As the aspect ratio $\mathscr{A}$ decreases, we observe a decrease in C_D (see Fig. 9). This trend is also apparent in the data of CF who studied $\mathscr{A} < 0.1$—a range more closely associated with ribbons and streamers.

Despite the fact that our C_D measurements are of the same order of magnitude and follow similar trends as those of CF, a slight vertical offset in the influence of $\mathscr{A}$ on C_D is evident—cf. Fig. 9 and the data sets corresponding to $\mathscr{A} = 0.43$ and CF's $\mathscr{A} = 0.1$ for example. Although the surface area of sheets considered by CF are $\mathscr{O}(10)$ smaller than those examined here, the mass ratios μ are quite similar for both studies ($\mu = 5.9 - 10.2$ for CF and $\mu = 6.4 - 15$ here). However, given that CF employs cotton flags, the reduced velocity range is of $\mathscr{O}(10^3)$ higher than the present study. This suggests a much greater influence on the response of the sheet from elastic deformations. As such, this may account for the slight vertical offset between the two data sets.

At small Reynolds numbers our measurements contain a degree of scatter which is generally reflected in the magnitude of the error bars. This uncertainty can be attributed to two factors: the small magnitude of the drag measured at small R; and the sensitivity of C_D to the sheet's orientation to the flow. For instance, as the flow velocity is increased the sheet assumes a number of stable non-oscillatory positions before aligning itself with the flow in a fully extended position. These changes in orientation affect the frontal and plane form area exposed to the flow and therefore, by consequence, the fluid drag. In other words, at low fluid velocities it is reasonable to expect that the memory or initial conditions of the system can influence the drag at subsequent fluid velocities before the sheet is fully extended. Once fully extended, we observe flutter.

An example, however, where a fully extended sheet remains stable to convected waves is demonstrated for S2 where $\mathscr{A} = 0.75$. Here, C_D exhibits two distinct regimes centred around a Reynolds number of $R \approx 4 \times 10^5$. This boundary corresponds to a sharp rise in C_D from 0.05 to 0.18 which approximates to a scaled flow velocity of $v/\mu \approx 30$. At this flow velocity the sheet loses stability to flutter (cf. Fig. 4(a)). A similar phenomenon is demonstrated by S4 with $\mathscr{A} = 0.5$, however, the rise in C_D is far less pronounced. For the remaining sheets, once fully extended in the flow, stability was lost immediately to flutter.

The measured results indicate that the drag experienced by the flag is generally of $\mathscr{O}(10)$ greater than that of flat plate of equal dimensions. Given the sheet's behaviour at small R before reaching a fully extended orientation in the flow, together with its flutter response at large R, this result not surprising. Within our range of Reynolds numbers, $\mathscr{O}(10^5 - 10^6)$, we can expect a turbulent boundary layer over the surface of the sheet. We notice that, like a flat plate, the drag coefficient decreases with increasing Reynolds number. However, the measurements indicate that this feature is perhaps more pronounced than that experienced by a flat plate. This would suggest that the boundary layer thickness is larger for a flexible sheet.

4.3. Fluid dynamic drag with in-plane tension

We now focus our attention on sheets S2, S3, and S4 and examine the fluid drag experienced by each in the presence of in-plane tension. We represent the magnitude of this tension by $\beta = T(L^2/B)$ which is applied at an angle θ to the trailing edge. For S2 and S3, the drag coefficient is presented for $\theta = 0°$ and $45°$ in Figs. 10 and 11, respectively. For S4, however, we consider an additional intermediate angle of $\theta = 22.5°$ and these data sets are shown in Fig. 12. For comparative purposes, the drag experienced by a flat (12) is plotted on each set of axes.

The measurements demonstrate a significant drag reduction through a moderate application of in-plane tension at the trailing edge. For example, S2 with $\beta > 0$ experiences a drag reduction by a factor of approximately $C_D/3$ when
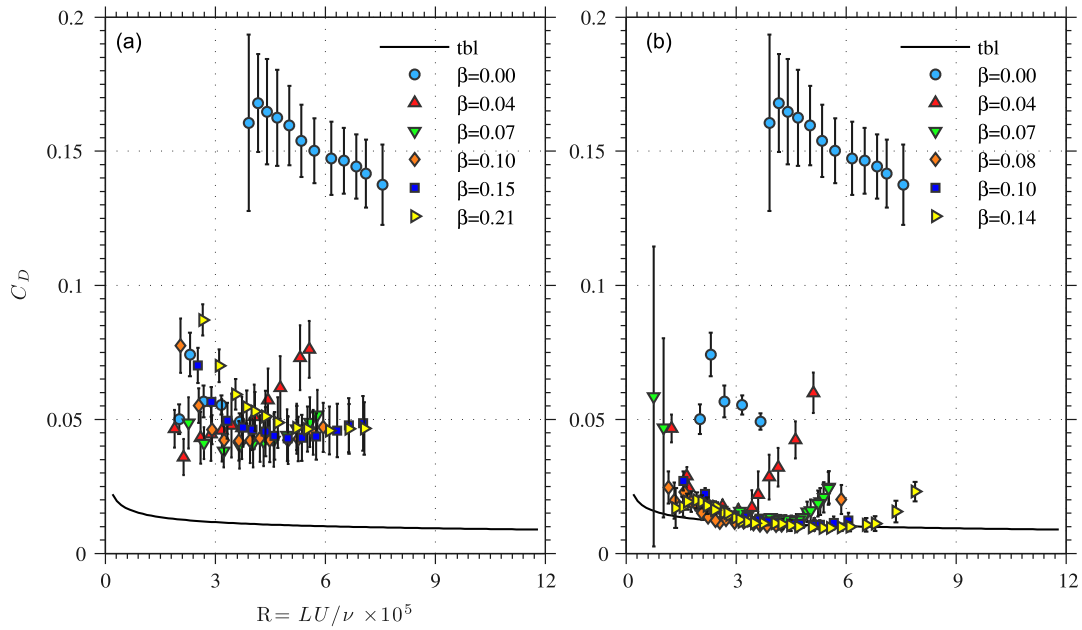
Fig. 10. The measured drag of S2 under constant tension $\beta = \kappa v^2(\times 10^6)$ in uniform flow. The subplots correspond to the trailing edge tension applied at angles: (a) $\theta = 0$; and (b) $\theta = 45°$. The error bars for each data point correspond to the standard deviation of C_D at each measured flow velocity. The solid line represents the drag on a flat plate, of $\mathscr{A} = 0.75$, experiencing a turbulent boundary layer.
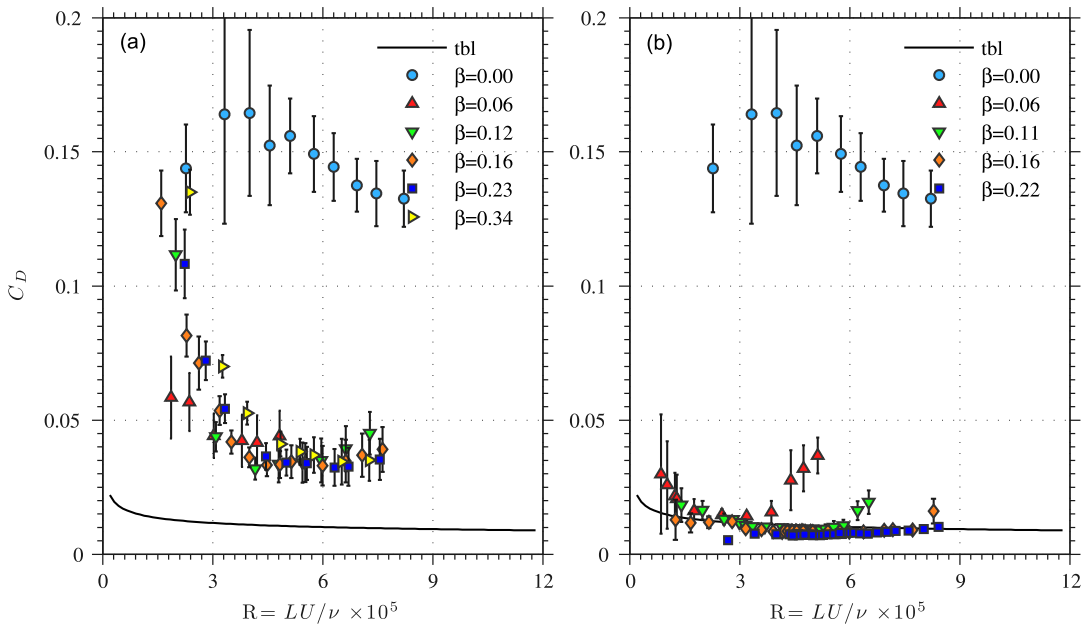

Fig. 11. The measured drag of S3 under constant tension $\beta = \kappa v^2(\times 10^6)$ in uniform flow. The subplots correspond to the trailing edge tension applied at angles: (a) $\theta = 0$ and (b) $\theta = 45°$. The error bars for each data point correspond to the standard deviation of C_D at each measured flow velocity. The solid line represents the drag on a flat plate, of $\mathscr{A} = 0.6$, experiencing a turbulent boundary layer.

compared to that of $\beta = 0$ (cf. Fig. 10). Moreover, such a dramatic reduction depends not only on the magnitude of the tension, but also on θ. To complicate matters further, stability also plays a crucial role. Distinctly different drag characteristics are observed before and after stability is lost to convected waves.
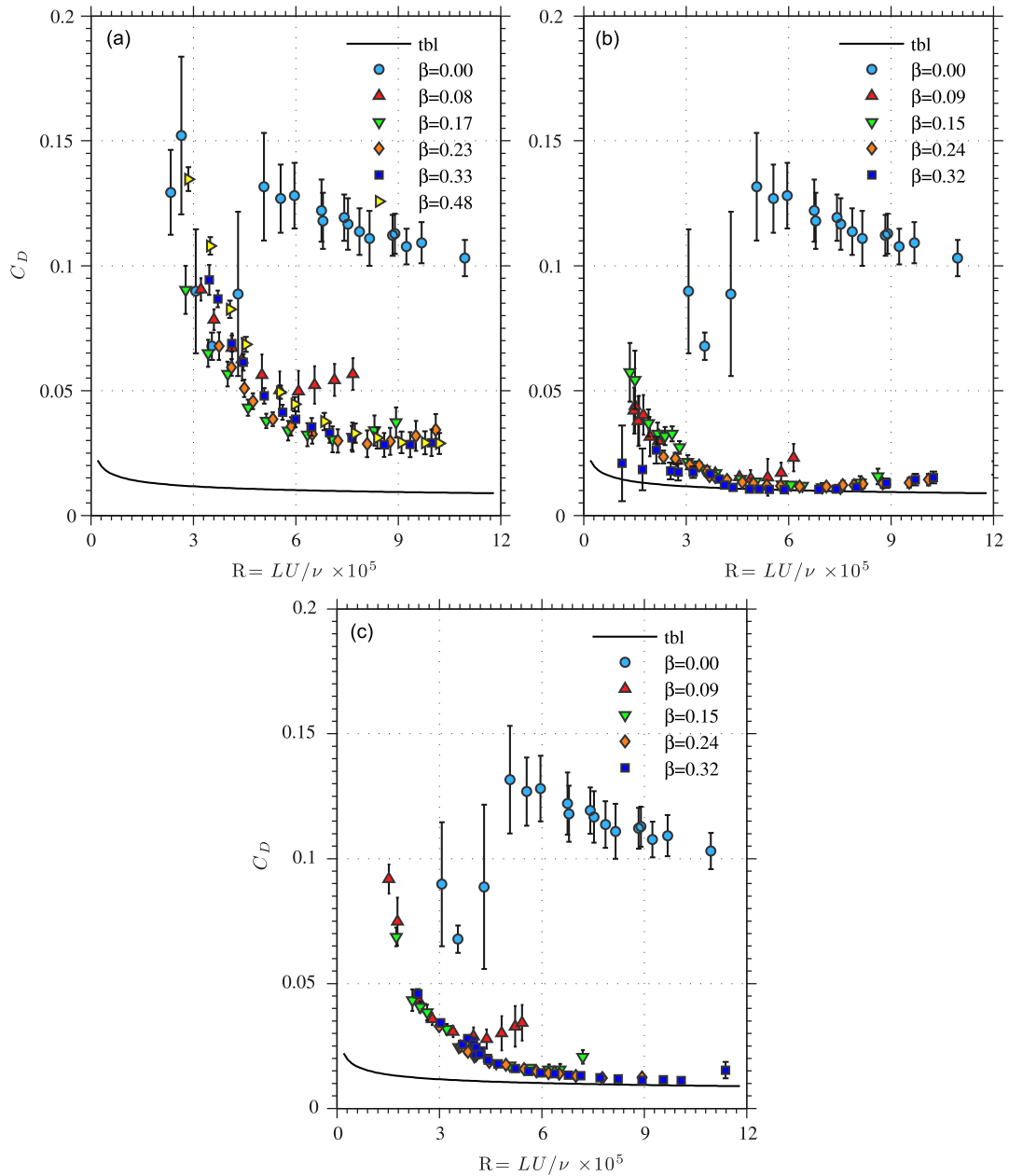
Fig. 12. The measured drag of S4 under constant tension $\beta = \kappa v^2 (\times 10^6)$ in uniform flow. The subplots correspond to the trailing edge tension applied at angles: (a) $\theta = 0$; (b) $\theta = 22.5°$; and (c) $\theta = 45°$. The error bars for each data point correspond to the standard deviation of C_D at each measured flow velocity. The solid line represents the drag on a flat plate, of $\mathscr{A} = 0.5$, experiencing a turbulent boundary layer.

Before instability $v < v_c$, the magnitude of C_D appears to be independent of $\beta > 0$. Provided sufficient in-plane tension is applied, the fluid drag of the sheet is reduced regardless of β (see Fig. 11(b) in particular). However, as θ increases the drag experienced by the sheet is further reduced. This behaviour is presumably caused by an improved and more streamlined orientation of the sheet—this relates to the discussion involving an increased fluid–elastic stability for increasing θ (cf. Section 4.1). This effect is best demonstrated in Fig. 12 for S4. At $\theta = 0$, the measured data is perhaps twice the C_D expected for a flat plate. While for $\theta = 22.5°$ and $45°$, the drag is reduced to such an extent that it is given to reasonable approximation by the flat plate drag law.

In contrast, for $v \geqslant v_c$, we observe that the in-plane tension plays a crucial role in the drag characteristics of the sheet. Ultimately, the magnitude of the in-plane tension dictates the critical fluid velocity, and the subsequent rise in the fluid drag once stability is lost. (cf. Fig. 10(b)). This explains the cascading behaviour of C_D, for increasing β during increasing Reynolds numbers, demonstrated in Figs. 10(b) and 11(b). Furthermore, these figures also suggest that the drag behaves in a linear fashion once stability is lost. In particular, we observe a sixfold escalation in C_D past the critical velocity for a moderate Reynolds number increase of 10^5. The convected wave response of the sheet is responsible for this dramatic drag increase once the critical velocity is breached. Although not indicated over the range of our data, one would expect that this linear increase in C_D to be arrested once the sheet performs chaotic motions and the coherent structures in the wake of the sheet breakdown [see Connell and Yue (2007), Fig. 23 and the related discussion]—this was not investigated here.

5. Conclusions

In the present work we have experimentally studied the drag and stability of a cantilevered flexible sheet in uniform flow characterised by $R = 10^4 - 10^6$. For the canonical case of a flag, we observe a decrease in the drag coefficient for decreasing aspect ratios within the range $0.43 < l/L < 1$—this agrees with previous studies. In the context of fluid drag and fluid–elastic stability, the notable feature of this present work has been an investigation into the effect of in-plane tension applied to the sheet. Our results indicate that the onset of a flutter-type instability can be delayed through the application of an in-plane tension. In particular, a monotonic increase in the critical velocity is observed for increasing tension. In the presence of in-plane tension, a dramatic reduction in the drag coefficient of the sheet is observed. The unique drag characteristics of the sheet are a corollary of its fluid–elastic stability. Interestingly, two regimes in the drag coefficient are seen, which appear to be separated by the critical velocity. Before stability is lost, the drag is well behaved and, provided transverse modes are suppressed, given to good approximation by the turbulent boundary layer drag law for a flat plate. However, once the sheet loses stability, the drag coefficient increases rapidly in a linear fashion with respect to the onset flow. The point at which this rapid increase occurs depends on the critical velocity and therefore the magnitude of the in-plane tension applied to the sheet.

References

Allen, J.J., Smits, A.J., 2001. Energy harvesting eel. Journal of Fluids and Structures 15, 629–640.

Argentina, M., Mahadevan, L., 2005. Fluid-flow-induced flutter of a flag. Proceedings of the National Academy of Sciences 102 (6), 1829–1834.

Auman, L.M., Dahlke, C.W., 2001. Drag characteristics of ribbons. In: Proceedings of the 16th Aerodynamic Decelerator Systems Technology Conference. AIAA, Boston, MA, pp. 131–136.

Auman, L.M., Wilks, B.L., 2005. Application of fabric ribbons for drag and stabilization. In: Proceedings of the 18th Aerodynamic Decelerator Systems Technology Conference. AIAA, Munich, Germany, pp. 1–9.

Carruthers, A.C., Filippone, A., 2005. Aerodynamic drag of streamers and flags. Journal of Aircraft 42 (4), 976–982.

Coene, R., 1992. Flutter of slender bodies under axial stress. Applied Scientific Research 49 (1), 175–187.

Connell, B.S.H., Yue, D.K.P., 2007. Flapping dynamics of a flag in a uniform stream. Journal of Fluid Mechanics 581, 33–67.

Crighton, D.G., Oswell, J.E., 1991. Fluid loading with mean flow. I. Response of an elastic plate to localized excitation. Philosophical Transactions: Physical Sciences and Engineering 335 (1639), 557–592.

Daniel, T.L., 1984. Unsteady aspects of aquatic locomotion. American Zoologist 24 (1), 121–134.

Datta, S.K., Gottenberg, W.G., 1975. Instability of an elastic strip hanging in an airstream. Journal of Applied Mechanics 75, 195–198.

Dowling, A.P., 1988. The dynamics of towed flexible cylinders. Part 1. Neutrally buoyant elements. Journal of Fluid Mechanics 187, 507–532.

Eloy, C., Souilliez, C., Schouveiler, L., 2007. Flutter of a rectangular plate. Journal of Fluids and Structures 23 (6), 904–919.

Fairthorne, R.A., 1930. Drag of flags. Reports and Memoranda, No. 1345, The Aeronautical Research Council, UK, pp. 887–891.

Farnell, D.J.J., David, T., Barton, D.C., 2005. Numerical model of self-propulsion in a fluid. Journal of the Royal Society Interface 2, 79–88.

Fitt, A.D., Pope, M.P., 2001. The unsteady motion of two-dimensional flags with bending stiffness. Journal of Engineering Mathematics 40, 227–248.

Hoerner, S.F., 1965. Fluid Dynamic Drag, second ed. Published by the author, New Jersey.

Huang, L., 1995. Flutter of cantilevered plates in axial flow. Journal of Fluids and Structures 9, 127–147.

Lamb, H., 1932. Hydrodynamics, sixth ed. Dover Publications, New York.

Lemaitre, C., Hémon, P., de Langre, E., 2005. Instability of a long ribbon hanging in axial air flow. Journal of Fluids and Structures 20 (7), 913–925.

Lighthill, M.J., 1960. Note on the swimming of slender fish. Journal of Fluid Mechanics 9, 305–317.

Morris-Thomas, M., Steen, S., 2008. The response of a flexible sheet under axial tension immersed in parallel flow. In: Proceedings of the 27th International Conference on Offshore Mechanics and Arctic Engineering. ASME, Estoril, Portugal, paper OMAE2008-57993.

Païdoussis, M.P., 2004. Fluid–Structure Interactions: Slender Structures and Axial Flow, vol. 2. Academic Press, San Diego, CA.

Rayleigh, L., 1879. On the instability of jets. Proceedings of the London Mathematical Society 10 (4), 4–13.

Schlichting, H., Gersten, K., 2000. Boundary Layer theory, eighth ed. Springer, London, UK.

Schouveiler, L., Eloy, E., Le Gal, P., 2005. Flow-induced vibrations of high mass ratio flexible filaments freely hanging in a flow. Physics of Fluids 17 (4), 047104.

Shelley, M., Vandenberghe, N., Zhang, J., 2005. Heavy flags undergo spontaneous oscillations in water. Physical Review Letters 94 (9), 1–4.

Souilliez, C., Eloy, C., Schouveiler, L., 2006. An experimental study of flag flutter. In: Proceedings of the Sixth FSI, AE and FIV + N Symposium at PVP2006. ASME, Vancouver, Canada, paper PVP2006-ICPVT11-93864.

Taneda, S., 1968. Waving motions of flags. Journal of the Physical Society of Japan 25 (2), 392–401.

Taneda, S., Tomonari, Y., 1974. An experiment on the flow around a waving plate. Journal of the Physical Society of Japan 36 (6), 1683–1689.

Tang, D.M., Yamamoto, H., Dowell, E.H., 2003. Flutter and limit cycle oscillations of two-dimensional panels in three-dimensional axial flow. Journal of Fluids and Structures 17 (2), 224–225.

Tang, L., Païdoussis, M.P., 2008. The influence of the wake on the stability of cantilevered flexible plates in axial flow. Journal of Sound and Vibration 310 (3), 512–526.

Watanabe, Y., Suzuki, S., Sugihara, M., Sueoka, Y., 2002. A experimental study of paper flutter. Journal of Fluids and Structures 16 (4), 529–542.

Wong, Y.W., Pellegrino, S., 2006. Wrinkled membranes. Part 1: experiments. Journal of Mechanics of Materials and Structures 1 (1), 3–25.

Yamaguchi, N., Ito, K., Ogata, M., 2003. Flutter limits and behaviors of flexible webs having a simplified basic configuration in high-speed flow. ASME Journal of Fluids Engineering 125 (2), 345–353.

Zhang, J., Childress, S., Libchaber, A., Shelley, M., 2000. Flexible filaments in a flowing soap film as a model for one-dimensional flags in a two-dimensional wind. Nature 408, 835–839.

Zhu, L., Peskin, C.S., 2002. Simulation of a flapping flexible filament in a flowing soap film by the immersed boundary method. Journal of Computational Physics 179, 452–468.